**WOOD RESEARCH** doi.org/10.37763/wr.1336-4561/71.2.331346
**e-ISSN 2729-8906**
**71(2): 2026 331-346 pp.**

# THE EXPERIMENTAL INVESTIGATION OF A MODEL OF A HISTORICAL-TYPE TIMBER ROOF SEGMENT UNDER PROGRESSIVE TIE-BEAM WEAKENING

JÁN BRODNIANSKY, SILVIA MARTINKOVIČOVÁ, JAROSLAV SANDANUS, TOMÁŠ KLAS
SLOVAK UNIVERSITY OF TECHNOLOGY IN BRATISLAVA
SLOVAK REPUBLIC

JIŘÍ KUNECKÝ, JIŘÍ BLÁHA, MICHAL KLOIBER
CZECH ACADEMY OF SCIENCES
CZECH REPUBLIC

(RECEIVED APRIL 2025)

## ABSTRACT

This paper reports on an experimental study of a model of a historical timber roof segment subjected to progressive weakening of the central tie beam. A three-frame specimen was tested under controlled loading, short-term sustained full load, and sequential cutting of the middle tie beam. Close-range photogrammetry was combined with inductive displacement sensors and conventional control measurements. The study examined the agreement of optical and contact measurements, redistribution of displacement demand to the adjacent frames, and the temporary residual stability provided by lathing after complete failure of the middle tie beam. Across the tie-beam midspans, the mean absolute difference between inductive and paired optical measurements ranged from 0.07 to 0.40 mm, with a maximum point-wise deviation of 1.39 mm. After complete failure, additional settlement of the two intact frames reached 4.28 and 3.97 mm relative to the pre-cut full-load state, indicating longitudinal redistribution through the lathing.

KEYWORDS: Historical timber roofs, tie-beam weakening, lathing, close-range photogrammetry, load redistribution.

## INTRODUCTION

Historical timber roof structures form an important part of the built heritage, yet their structural assessment remains difficult due to material variability, long-term degradation, hidden defects, and repeated interventions carried out during the service life of the building (Yeomans 2003, Branco et al. 2014, Binda and Saisi 2005, Jasieńko et al. 2016, Ross 2015).

Local damage to a major element may substantially alter stiffness, internal force transfer, and the overall stability of the roof system (Stepinac et al. 2017, Nowak et al. 2013). Experimental investigation is therefore valuable in the diagnosis of historical timber structures, as it allows the actual response of the system to be observed for the verification of structural assumptions used in rehabilitation design (Dinehart and Shenton 1998, Frese et al. 2012, Reynders et al. 2010). In this context, close-range photogrammetry and contact displacement sensing are suitable tools for recording both global and local deformations of a timber roof model (Remondino 2011, Fassi et al. 2013, Luhmann et al. 2013, Mills et al. 2010). Comparable optical and digital-image-correlation approaches have been validated against conventional contact measurements on timber members and carpentry joints (Li et al. 2022, Kunecký et al. 2015, Hu et al. 2021).

For historical timber roofs, the work on automated point-cloud-based reconstruction and uncertainty-aware finite-element modelling further emphasizes the importance of reliable geometric survey and system-level interpretation before structural assessment (Özkan et al. 2022, Zybała et al. 2022). Full-scale studies on historic timber trusses also showed that joint behaviour and global structural response should be evaluated together when damage and repair strategies are discussed (Munafò et al. 2015, Branco et al. 2014). Recent experiments have addressed structural timber problems closely related to load-displacement behaviour of nailed and screwed truss joints (Moya and Tenorio 2017), flexural response and lateral stability of reinforced wood trusses (Yang et al. 2020), and semi-rigid timber connections verified experimentally and numerically (Neusch et al. 2022).

A specific issue is the role of lathing in the longitudinal redistribution of load when one transverse frame is weakened. Although lathing is often treated primarily as a secondary component of the roof covering, the broader research work behind this study indicated that it may contribute significantly to the stiffness and redundancy of the system, particularly under damage conditions (Martinkovičová 2025). For this reason, the simplified experimental model was designed to emphasize the interaction between the weakened frame and the adjacent intact frames through the lathing. As the reference structure, the roof above the presbytery of the Church of the Annunciation of the Virgin Mary in Cheb, Czech Republic, was selected. A model of a roof segment with three transverse frames was prepared. The maximum element length was limited to 3 m for fabrication and handling reasons, and the central tie beam was progressively weakened by cutting. The study focuses on comparing optical and contact systems used for deformation monitoring.

Stated explicitly, the paper has two aims: *(i)* to verify close-range photogrammetry against inductive displacement sensors as parallel measurement systems on a single timber roof model, and *(ii)* to use these measurements to document the longitudinal load redistribution provided by the lathing when the central tie beam is progressively weakened and finally severed.

## MATERIAL AND METHODS

### Experimental model

The model was fabricated from carefully selected spruce timber and prepared at the Institute of Theoretical and Applied Mechanics in Telč (Fig. 1). The broader experimental

framework, subsequent material testing, and numerical calibration are described in Martinkovičová (2025), whereas the present paper isolates the experimental configuration and procedure. The principal geometric parameters, verified dimensions, and ballast characteristics are summarized in Tab. 1. To prevent unintended global horizontal movement, the model was additionally stabilized at the apex by tension straps. In Tab. 1, the nominal (target) value is the design dimension specified for fabrication, whereas the verified value is the dimension measured on the completed specimen before testing; the comparison documents the fabrication tolerances and confirms that the as-built geometry matches the design assumptions.

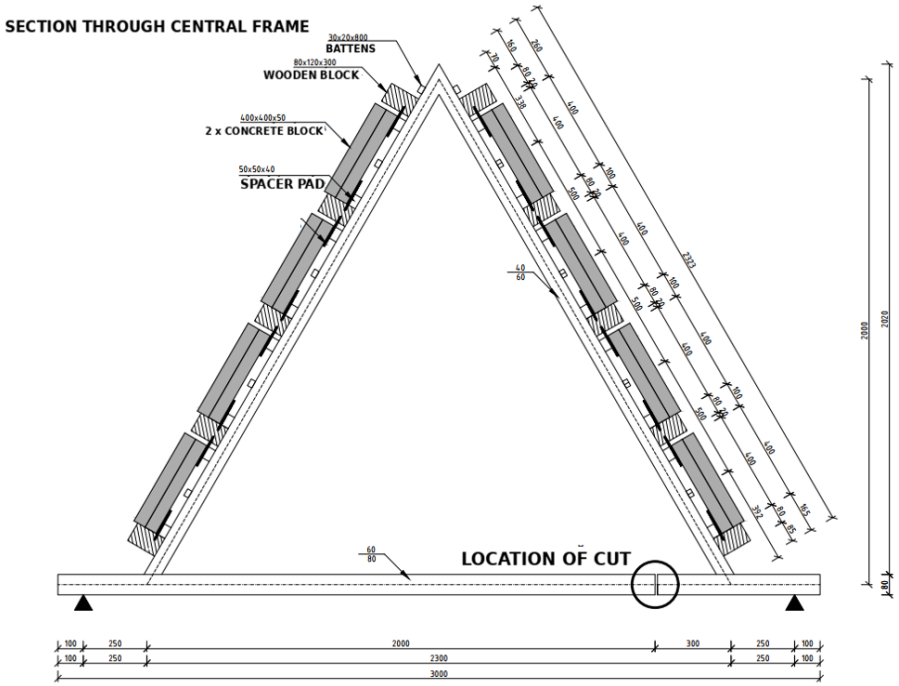


*Fig. 1: Section through the central transverse frame — element dimensions in mm, lathing, wooden spacer blocks, concrete-block ballast (applied load) and the location of the tie-beam cut.*

*Tab. 1: Element dimensions and layout parameters.*

| Item | Nominal or target value | Verified value / arrangement |
|---|---|---|
| Tie beam cross-section | 60 × 80 mm | mean measured 59.24 × 79.51 mm |
| Rafter cross-section | 40 × 60 mm | mean measured 39.78 × 59.67 mm |
| Batten cross-section | 20 × 30 mm | mean measured about 20.00 × 29.85 mm |
| Support axis distance | 2800 mm | measured about 2805 mm (2723 mm between inner faces of wall plates) |
| Spacing of transverse frames | 400 mm | clear spacing between tie beams 341–345 mm and 341–342 mm (measured between inner faces of the tie beams) |
| Batten spacing | 500 mm; ridge batten 350 mm | clear spacing 468–477 mm and 319–326 mm (measured between inner faces of the battens) |
| Loading blocks | 400 × 400 × 50 mm; declared 16.8 kg | average checked mass 18.2 kg |

The model elements were fabricated from spruce (*Picea abies*) (Fig. 2). For all structural calculations the timber was assumed to be strength class C27 with characteristic values

according to STN EN 338; visual/mechanical grading follows STN EN 14081-1 and characteristic values are derived per STN EN 384. The global modulus of elasticity of the individual element groups was verified experimentally according to STN EN 408 (Tab. 7). On this basis the post-test classification was approximately C45 for the battens, C35 for the rafters and C27 for the tie beams.

The fixed support of the structure was achieved by bolting the structure to a 60 × 80 mm wall plate. The sliding support was formed by rollers placed on a second wall plate, with steel plates inserted to avoid local indentation. Both wall plates were carried by steel supports that provided the required elevation of the model and were additionally loaded to prevent unintended movement.

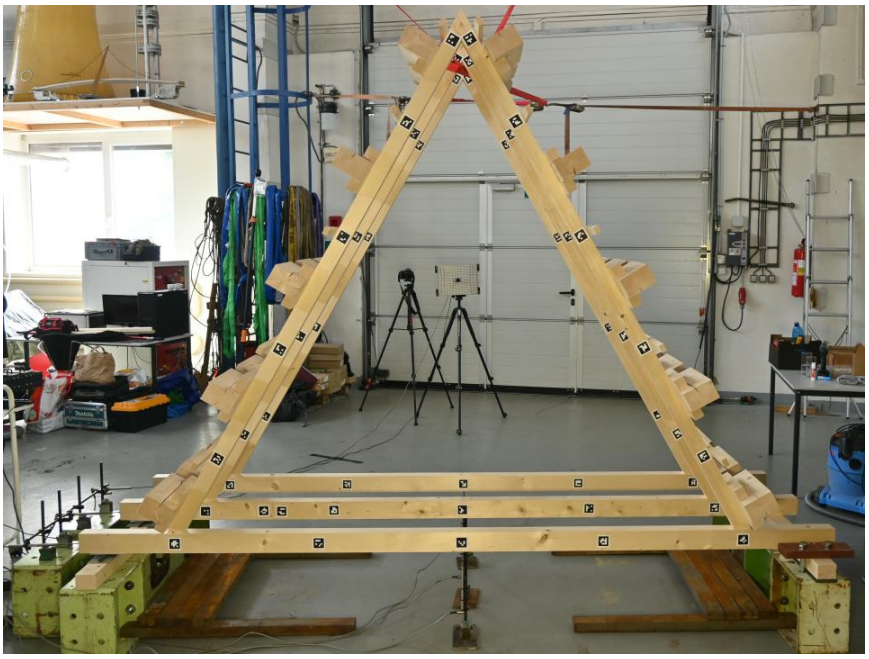

*Fig. 2: Experimental model with optical (ArUco) targets.*

The design spacing of the transverse frames was 400 mm centre to centre. When the 60 mm width of the tie beams is taken into account, the measured clear distances showed good agreement with the design. The battens were arranged at 500 mm centre-line spacing in the intermediate zones and at 350 mm at the ridge. Loading was applied by concrete blocks placed in pairs in four rows on both roof planes so that each of the three frames carried a nominally equal share of the applied load. Wooden spacer blocks of 80 × 120 × 300 mm and anti-overturning battens of 50 × 40 × 250 mm were screwed to the rafters. The main carpentry joints relevant to the experiment were provided as a mortise-and-tenon connection between the rafter and the tie beam, a half-lap joint with a wooden dowel at the apex, and nailed batten connections. From the viewpoint of the present study, the batten-to-rafter connection was particularly important; it was made with nails 2.5 × 60 mm.

**Measurement system**

The response of the model was monitored by a combination of close-range photogrammetry, inductive displacement sensors, and conventional control measurements

performed with a tape measure and a laser distance meter. The conventional measurements were used for geometric verification during assembly and for spot-checking selected distances in the evaluation sheets; they were not used as a continuous displacement-recording system. This combined setup was selected so that global deformation of the roof segment and local movements of the tie beams could be checked independently and then compared.

*Photogrammetric measurement*

Optical measurement was based on printed ArUco fiducial markers measuring 4 × 4 cm, selected because they provide uniquely coded targets suitable for robust automatic detection (Garrido-Jurado et al. 2014). On the rafters, the markers were placed beneath the battens at 500 mm spacing, and on the tie beams at 560 mm spacing. Targets were attached on both sides of the members, and additional markers were placed near the intended cut in the central tie beam. The transverse label PC denotes the side of the specimen adjacent to the sliding support. The marker layouts visible from the two camera positions are shown in Fig. 3.

Image acquisition was performed by two Basler acA2440-20gm cameras with 5 MP resolution. Cam1 was located on the laboratory side of the specimen and Cam2 on the entrance side. Each target received a unique identifier related to its longitudinal position (entrance, middle, laboratory) and transverse orientation, and a total of 46 optical points were evaluated. Camera calibration was carried out using A3 1200-DPI chessboards glued to glass (11 × 15 pattern) from multiple views at a working distance of approximately 2 m. Because the principal-point coordinates cx and cy remained close to the image centre, the distortion coefficients obtained in calibration were preserved for the laboratory configuration and only the focal length was re-estimated. Marker identification and coordinate extraction were implemented in OpenCV (Bradski 2000). The complete key of the optical markers (camera, ID, element and position on the model) is given in Tab. 2.

*Tab. 2: Optical marker key — camera, ID, element and position on the model.*

| No. | Camera | ID | Element | Position on the model | No. | Camera | ID | Element | Position on the model |
|---|---|---|---|---|---|---|---|---|---|
| 1 | Cam1 | ID_48 | Rafter – laboratory frame | 2nd from bottom, PC side | 24 | Cam1 | ID_99 | Tie beam – middle frame | at the cut, entrance side |
| 2 | Cam1 | ID_50 | Tie beam – laboratory frame | PC side–centre | 25 | Cam2 | ID_5 | Rafter – entrance frame | 2nd from bottom, entrance side |
| 3 | Cam1 | ID_54 | Rafter – laboratory frame | 3rd from bottom, PC side | 26 | Cam2 | ID_6 | Tie beam – entrance frame | centre |
| 4 | Cam1 | ID_56 | Tie beam – laboratory frame | centre | 27 | Cam2 | ID_8 | Rafter – entrance frame | 1st from bottom, entrance side |
| 5 | Cam1 | ID_57 | Rafter – laboratory frame | 1st from bottom, PC side | 28 | Cam2 | ID_9 | Tie beam – entrance frame | entrance side |
| 6 | Cam1 | ID_58 | Rafter – laboratory frame | 3rd from bottom, entrance side | 29 | Cam2 | ID_11 | Rafter – entrance frame | 3rd from bottom, PC side |
| 7 | Cam1 | ID_59 | Tie beam – laboratory frame | PC side | 30 | Cam2 | ID_12 | Tie beam – entrance frame | centre–entrance |
| 8 | Cam1 | ID_60 | Tie beam – middle frame | PC side–centre | 31 | Cam2 | ID_13 | Rafter – entrance frame | 3rd from bottom, entrance side |
| 9 | Cam1 | ID_62 | Tie beam – middle frame | PC side | 32 | Cam2 | ID_17 | Tie beam – middle frame | centre–entrance |
| 10 | Cam1 | ID_63 | Rafter – middle frame | 1st from bottom, PC side | 33 | Cam2 | ID_18 | Rafter – middle frame | 2nd from bottom, entrance side |
| 11 | Cam1 | ID_64 | Rafter – middle frame | 3rd from bottom, PC side | 34 | Cam2 | ID_20 | Rafter – middle frame | 1st from bottom, entrance side |
| 12 | Cam1 | ID_66 | Tie beam – middle frame | centre | 35 | Cam2 | ID_24 | Rafter – middle frame | 3rd from bottom, entrance side |
| 13 | Cam1 | ID_68 | Rafter – middle frame | 3rd from bottom, entrance side | 36 | Cam2 | ID_26 | Tie beam – middle frame | centre |
| 14 | Cam1 | ID_72 | Rafter – middle frame | 2nd from bottom, PC side | 37 | Cam2 | ID_28 | Rafter – middle frame | centre |

| | | | | | | | | | |
|---|---|---|---|---|---|---|---|---|---|
| 15 | Cam1 | ID_75 | Rafter – entrance frame | centre | 38 | Cam2 | ID_29 | Tie beam – middle frame | entrance side |
| 16 | Cam1 | ID_76 | Tie beam – entrance frame | PC side | 39 | Cam2 | ID_30 | Rafter – laboratory frame | 3rd from bottom, entrance side |
| 17 | Cam1 | ID_79 | Tie beam – entrance frame | PC side–centre | 40 | Cam2 | ID_31 | Rafter – laboratory frame | 2nd from bottom, entrance side |
| 18 | Cam1 | ID_82 | Tie beam – entrance frame | centre | 41 | Cam2 | ID_32 | Rafter – laboratory frame | 1st from bottom, entrance side |
| 19 | Cam1 | ID_83 | Rafter – entrance frame | 3rd from bottom, entrance side | 42 | Cam2 | ID_35 | Tie beam – laboratory frame | PC side–centre |
| 20 | Cam1 | ID_85 | Tie beam – entrance frame | centre–entrance | 43 | Cam2 | ID_39 | Tie beam – laboratory frame | centre |
| 21 | Cam1 | ID_86 | Rafter – entrance frame | PC side–centre | 44 | Cam2 | ID_40 | Tie beam – laboratory frame | centre–entrance |
| 22 | Cam1 | ID_89 | Rafter – entrance frame | PC side | 45 | Cam2 | ID_41 | Tie beam – laboratory frame | entrance side |
| 23 | Cam1 | ID_98 | Tie beam – middle frame | at the cut, PC side | 46 | Cam2 | ID_43 | Rafter – laboratory frame | 3rd from bottom, PC side |

The present paper evaluates relative displacements between individual measurement steps rather than absolute global coordinates. Measurement No. 1 defined the reference configuration. At each subsequent step, 100 images were acquired and the extracted coordinates were averaged to suppress random image noise. Validation of the photogrammetric setup was performed a posteriori at the three tie-beam midspans, where optical points coincided with inductive sensors. During the loading phase, the comparison yielded MAE values of 0.07–0.40 mm and RMSE values of 0.08–0.49 mm, while the maximum point-wise deviation was 1.39 mm for the most distant marker recorded by Cam2. Some peripheral markers were slightly blurred because the whole specimen had to be captured from fixed camera positions; however, the central tie-beam points and the weakened middle frame remained within the best-resolved part of the image set.

MAE denotes the mean absolute error and RMSE the root-mean-square error between the optical and inductive displacement values at the paired points; both are reported in millimetres.

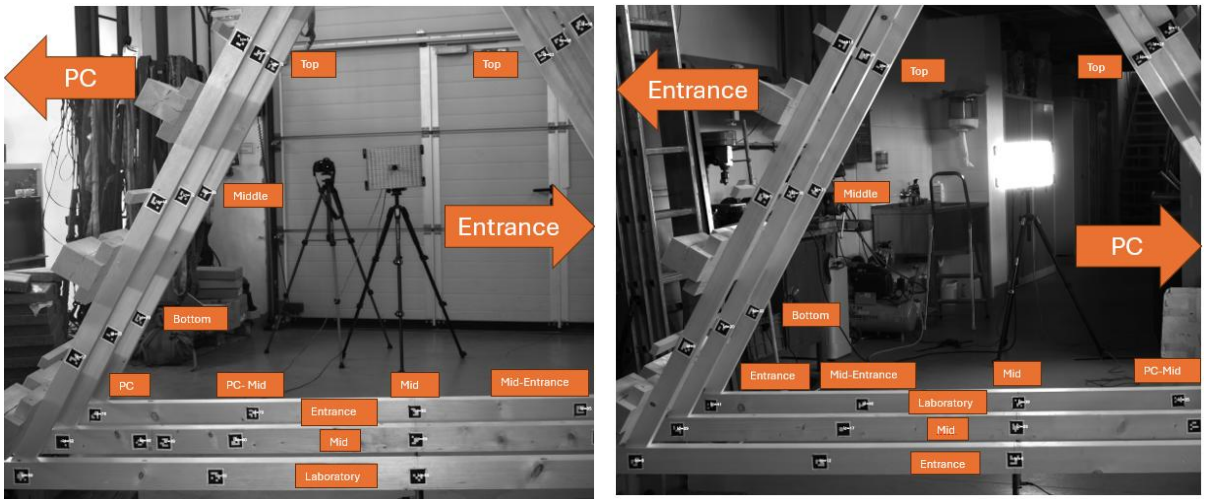


*Fig. 3: (left) Optical targets recorded by Cam1 from the laboratory side; (right) Optical targets recorded by Cam2 from the entrance side*

*Inductive displacement sensors*

As a second measurement system, a Spider8 unit equipped with six inductive displacement sensors was used. Three vertical sensors recorded deflections at the centres of the three tie

beams, while three horizontal sensors recorded movements in the corresponding horizontal positions of the individual frames. The sensor arrangement allowed direct comparison between the contact measurements and the optical points located at the tie-beam centres; the adopted correspondence is summarized in Tab. 3. The six inductive sensors carry the orientation suffix V (vertical) or H (horizontal); the three vertical sensors I4V, I5V and I6V measure the midspan deflection of the three tie beams, and each is paired with the two optical markers flanking the same midspan (I4V with ID_56/ID_39, I5V with ID_66/ID_26, I6V with ID_82/ID_6), which form the basis of the optical–contact comparison in Tab. 5.

*Tab. 3: Inductive displacement sensors and correspondence with optical points.*

| Sensor | Location | Recorded quantity | Optical point correspondence |
|---|---|---|---|
| I1 H | Tie beam – laboratory frame, horizontal position | Horizontal displacement | — |
| I2 H | Tie beam – middle frame, horizontal position | Horizontal displacement | — |
| I3 H | Tie beam – entrance frame, horizontal position | Horizontal displacement | — |
| I4 V | Tie beam – laboratory frame, centre | Vertical displacement | ID_56 / ID_39 |
| I5 V | Tie beam – middle frame, centre | Vertical displacement | ID_66 / ID_26 |
| I6 V | Tie beam – entrance frame, centre | Vertical displacement | ID_82 / ID_6 |

**Loading scenario and test sequence**

The measurement scenario was adapted to laboratory operation. The complete test consisted of 27 measurement steps grouped into three phases: loading, sustained full load, and failure. Loading started from the unloaded reference state and continued by gradual placement of ballast above the movable support, unloading, repetition above the fixed support, and three combined full-load states. The sustained full-load phase comprised six measurements before cutting, with the last record taken 12,355 s after the reference measurement. The complete sequence is summarized in Tab. 4.

Failure was introduced by progressive cutting of the central tie beam in increments of 2, 4, 6, and 7 cm, followed by a full cut. Two additional final states were then recorded before the induced collapse, namely the stage labelled “before collapse” and the stage with the half-cut entrance tie beam, and the sequence ended with the collapse step. All phases were documented by photographs, videos, and written notes.

The cut increments 2, 4, 6 and 7 cm denote the depth of the saw cut into the 80 mm height of the central tie beam (cross-section 60 × 80 mm, Tab. 1), measured from the lower (tension) face; the “full cut” severs the remaining ligament. Tab. 4 lists, for each of the 27 steps, the elapsed time, the action performed (Description) and the phase, so the loading and failure procedure can be followed step by step.

*Tab. 4: Sequence of measurement.*

| Step | Elapsed time [s] | Description | Phase |
|---|---|---|---|
| 1 | 0 | No load | Loading |
| 2 | 130 | First row above movable support | Loading |
| 3 | 240 | Second row above movable support | Loading |
| 4 | 361 | Third row above movable support | Loading |
| 5 | 522 | Fourth row above movable support | Loading |
| 6 | 760 | Unloading | Loading |

| Step | Elapsed time [s] | Description | Phase |
|---|---|---|---|
| 7 | 859 | First row above fixed support | Loading |
| 8 | 958 | Second row above fixed support | Loading |
| 9 | 1072 | Third row above fixed support | Loading |
| 10 | 1186 | Fourth row above fixed support | Loading |
| 11 | 1328 | Full fixed + 1 movable | Loading |
| 12 | 1414 | Full fixed + 2 movable | Loading |
| 13 | 1513 | Full fixed + 3 movable | Loading |
| 14 | 1633 | Full 1 | Sustained full load |
| 15 | 2253 | Full 2 | Sustained full load |
| 16 | 2667 | Full 3 | Sustained full load |
| 17 | 5237 | Full 4 | Sustained full load |
| 18 | 11764 | Full 5 | Sustained full load |
| 19 | 12355 | Full 6 before cutting | Sustained full load |
| 20 | 12645 | 2 cm cut | Failure |
| 21 | 12784 | 4 cm cut | Failure |
| 22 | 12938 | 6 cm cut | Failure |
| 23 | 13401 | 7 cm cut | Failure |
| 24 | 13613 | Full cut | Failure |
| 25 | 15088 | Before collapse | Failure |
| 26 | 15210 | Half-cut entrance tie beam | Failure |
| 27 | 15329 | End collapse | Failure |

### Data processing

All measured data were processed in MS Excel. The optical dataset contained 46 points with XYZ coordinates evaluated in 27-time records, which corresponds to approximately 3700 coordinate outputs. The sensor dataset comprised 5300 records in the loading phase at 2 Hz, 9800 records in the sustained full-load phase at 1 Hz, and 7990 records in the failure phase at 2 Hz. Measurement No. 1 (no load) was taken as the reference state and all subsequent displacements were evaluated relative to it. The evaluation sheets combined point positions, camera assignment, distances within one transverse frame and between frames, the time of the selected measurement, and the corresponding photo documentation. For the three tie-beam midspans, additional paired datasets were prepared for direct comparison between I4V and ID_56/ID_39, I5V and ID_66/ID_26, and I6V and ID_82/ID_6.

In each paired dataset the contact deflection from the vertical inductive sensor is compared with the mean of the two optical markers on the same beam; all three comparison locations lie at the centre of the respective tie beam.

## RESULTS AND DISCUSSION

### Agreement of optical and inductive measurements during loading

The comparison of optical targets and inductive displacement sensors at the midspans of the tie beams showed close agreement throughout the loading phase. Tab. 5 summarizes the differences between the inductive records and the paired optical points for measurement steps 1–19, and Fig. 4 plots the corresponding displacement histories for the three tie-beam midspans. When the two optical observations of the same physical point were averaged, the mean absolute difference ranged from 0.07 to 0.40 mm and the RMSE from 0.08 to

0.49 mm. The largest point-wise absolute difference, 1.39 mm, occurred for ID_39 at measurement step 17, i.e. for the most distant marker seen by Cam2. Despite this local deviation, all three measurement traces captured the same loading history and the same order of stiffness among the frames. Under the same loading level, the middle tie beam exhibited the largest vertical deflection, the entrance tie beam the smallest one, and the laboratory-side tie beam an intermediate response.

*Tab. 5: Summary of the agreement between optical and inductive measurements during loading.*

| Frame | Compared data | MAE of averaged optical vs inductive [mm] | RMSE [mm] | Maximum point-wise absolute difference [mm] |
|---|---|---|---|---|
| Laboratory-side | I4V vs ID_56 / ID_39 | 0.40 | 0.49 | 1.39 (ID_39, step 17) |
| Middle | I5V vs ID_66 / ID_26 | 0.07 | 0.11 | 0.43 (ID_26, step 17) |
| Entrance-side | I6V vs ID_82 / ID_6 | 0.07 | 0.08 | 0.47 (ID_6, step 17) |

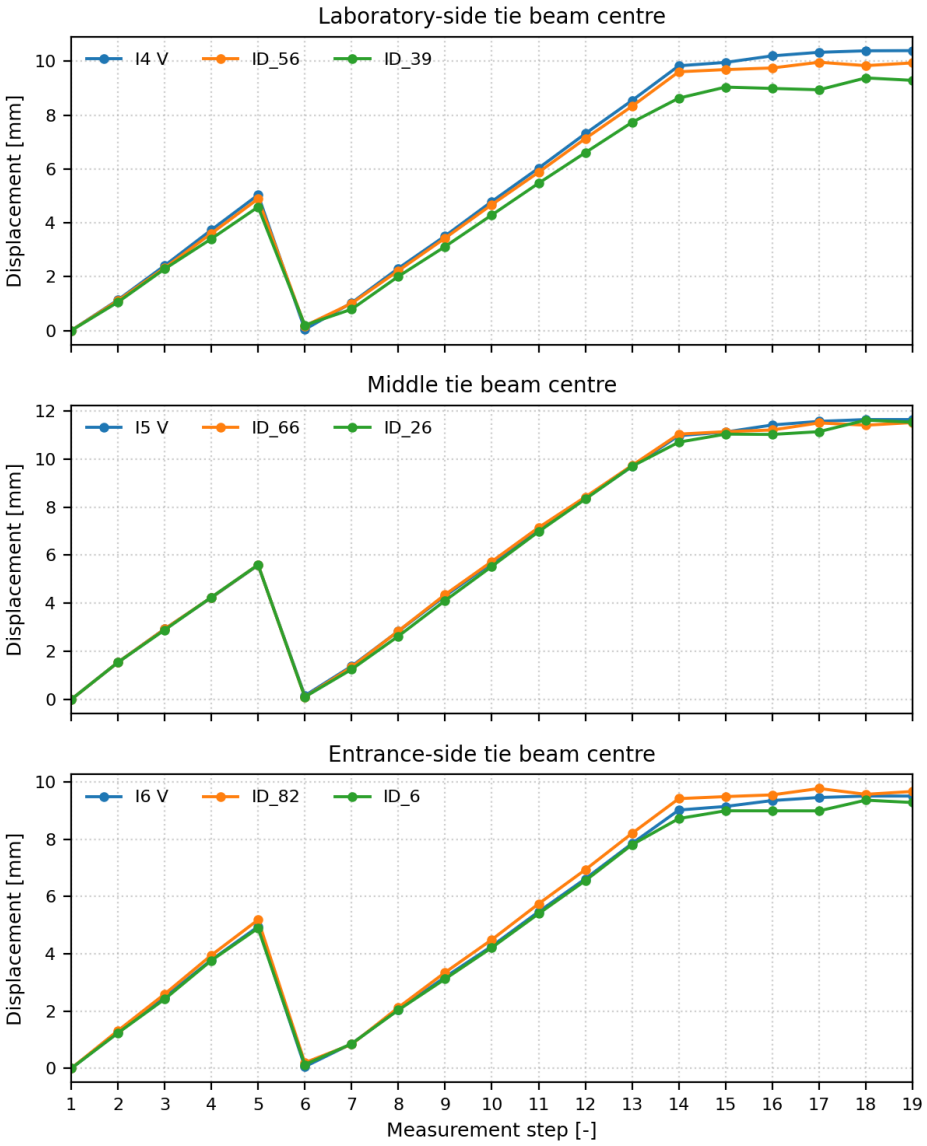


*Fig. 4: Comparison of optical and inductive measurements at the tie-beam midspans during loading.*

The rafter points also showed mutually consistent displacement histories, although slightly larger deviations appeared at points that were partly obscured or located deeper in the viewing direction. The measurements of horizontal displacements confirmed that the global lateral movement of the model remained very small, with a maximum value of approximately 1 mm. The observed response can therefore be interpreted predominantly as a consequence of vertical deformation and local stiffness differences rather than rigid-body translation of the entire specimen.

**Progressive cutting of the central tie beam**

The stage of progressive weakening was evaluated from measurement 19, taken as the fully loaded reference state before cutting, to measurement 24, corresponding to the full cut of the central tie beam. The additional settlements recorded during this phase are plotted in Fig. 5. At the first cut increment (2 cm), the additional settlements relative to the reference state were still small: 0.16 mm in the laboratory-side frame, 0.13 mm in the middle frame, and 0.09 mm in the entrance-side frame. At step 22 (6 cm cut), the corresponding additional settlements increased to 1.48, 3.98, and 1.33 mm, and at step 23 (7 cm cut) to 2.39, 7.26, and 2.13 mm. After the full cut (step 24), the laboratory-side and entrance-side frames showed very similar additional settlements of 4.28 and 3.97 mm, whereas the middle frame jumped to 44.67 mm. Up to the stage of complete failure of the central tie beam, this behaviour indicates a nearly symmetric redistribution of load from the weakened middle frame to the two side frames through the lathing.

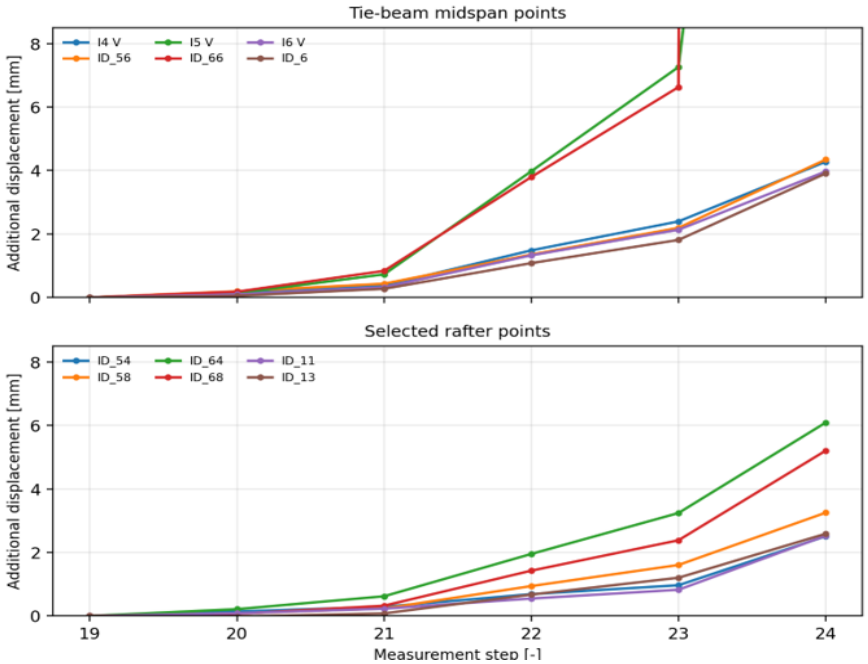


*Fig. 5: Additional displacement during progressive cutting of the central tie beam.*

A detailed evaluation of the opening of the cut was carried out using the displacement of points ID_98 and ID_99 located at the weakened section. Their relative movement increased monotonically with cut depth, and the corresponding opening angle calculated from the optical

data was in agreement with inclinometer control measurements. This confirms that the adopted measurement strategy was sufficiently sensitive not only to global displacements of the frames but also to the local opening mechanism that developed in the damaged tie beam. The largest local displacements were recorded at rafter points ID_64 and ID_68 on the middle frame, i.e. in the region closest to the cut.

**Short-term response under sustained full load**

The fully loaded state was monitored between measurements 14 and 19, corresponding to 10,722 s (2 h 58 min 42 s). Additional settlement relative to measurement 14 remained limited: by measurement 19 the vertical sensors recorded increases of 0.56 mm, 0.67 mm, and 0.49 mm in the laboratory-side, middle, and entrance-side frames, respectively. The values developed gradually and without any abrupt change, which indicates a stable short-term response under sustained load. Because these increments were only in the order of tenths of a millimetre, the small differences between optical and inductive measurements became more visible than in the main loading phase. The corresponding sensor-based increments are summarized in Tab. 6.

*Tab. 6: Additional settlement during the sustained full-load phase relative to Measurement No. 14.*

| Measurement step | Laboratory-side I4V [mm] | Middle I5V [mm] | Entrance-side I6V [mm] |
|---|---|---|---|
| 14 | 0.00 | 0.00 | 0.00 |
| 15 | 0.13 | 0.15 | 0.13 |
| 16 | 0.37 | 0.44 | 0.33 |
| 17 | 0.50 | 0.59 | 0.44 |
| 18 | 0.56 | 0.67 | 0.49 |
| 19 | 0.56 | 0.67 | 0.49 |

**Final phase after complete failure of the central tie beam**

After the central tie beam had been cut through completely, the experimental model did not collapse immediately. Instead, the damaged middle frame remained temporarily suspended by the lathing, which enabled further transfer of load to the two intact side frames. The displacement development in the last self-supporting stage is summarized in Fig. 6. Relative to the fully loaded pre-cut state (step 19), the middle frame reached an additional settlement of 44.67 mm at step 24, while the laboratory-side and entrance-side frames reached only 4.28 and 3.97 mm. Measurements 25 and 26 showed that the middle frame remained at approximately the same additional settlement level, whereas the two intact frames changed only modestly until the entrance tie beam was deliberately half-cut.

Measurement 26 was the last stage that could still be described as self-supporting. At this stage, the laboratory-side and entrance-side frames showed additional settlements of 5.34 mm and 7.24 mm, respectively, while the middle frame remained at 44.66 mm relative to step 19. In measurement 27 the specimen had already been additionally suspended at the apex, and a controlled collapse was triggered by half-cutting the entrance tie beam. The final sequence therefore demonstrates that complete loss of the middle tie beam alone was not sufficient to produce immediate collapse of the three-frame system; the decisive failure state developed only after the redundancy created by the adjacent intact frame was further reduced.

**Selected post-test material properties relevant to interpretation**

Post-test material measurements from the broader study help explain the non-identical response of the three frames and the longitudinal action of the battens. Selected values directly relevant to the present interpretation are summarized in Tab. 7. The entrance-side tie beam was stiffer than the other two tie beams, while the battens showed the highest stiffness and bending resistance among the tested element groups. The global moduli of elasticity of the three tie beams are listed in Tab. 7 (9.8, 10.0 and 12.4 GPa for the laboratory-side, middle and entrance-side frame; group mean 10.8 GPa, 5% quantile 9.8 GPa, i.e. class C27), whereas the 5% quartile of bending strength is given only for the rafters (57.5 MPa) and battens (69.7 MPa) because the tie beams were not loaded to rupture.

*Tab. 7: Selected post-test material properties relevant to the interpretation of the experimental response.*

| Element | Mean global modulus of elasticity [GPa] | 5% quartile of bending strength [MPa] |
|---|---|---|
| Tie beam – laboratory-side | 9.8 | — |
| Tie beam – middle | 10.0 | — |
| Tie beam – entrance-side | 12.4 | — |
| Rafters | 12.5 | 57.5 |
| Battens | 15.2 | 69.7 |

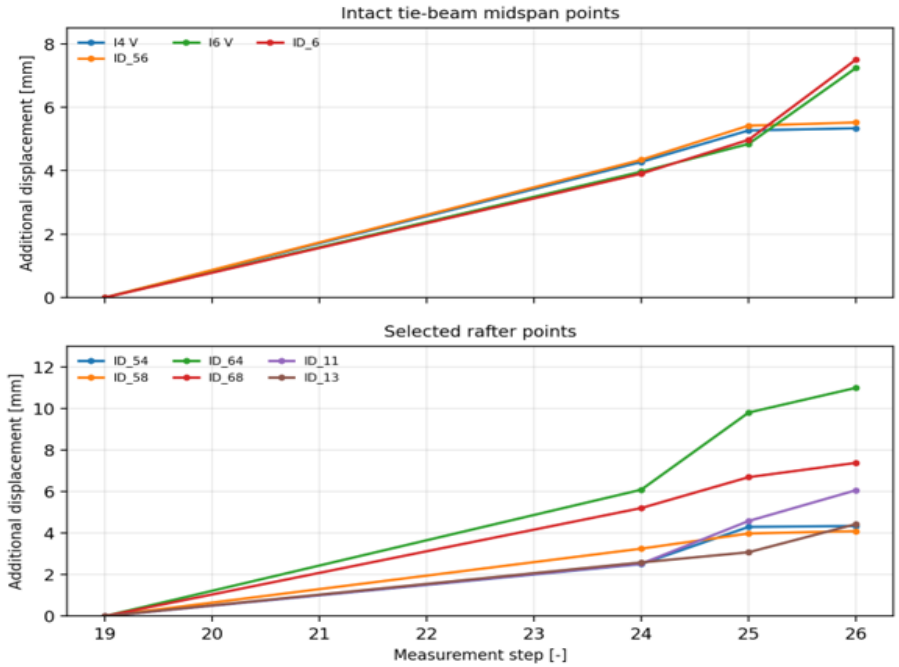


*Fig. 6: Final self-supporting phase after complete failure of the central tie beam.*

**Discussion**

Although the present paper remains primarily experimental, the selected results support one mechanism-oriented conclusion. In the present laboratory configuration, the battens did not act merely as a secondary support for a hypothetical roof covering, but as an active longitudinal load-transfer path between the three frames. This interpretation is supported by two independent observations documented in Fig. 5 and Fig. 6. First, the two intact side frames showed nearly

symmetric additional settlements during progressive weakening up to the stage of full cut. Second, the system remained temporarily self-supporting after complete failure of the middle tie beam, which would not be possible without residual load transfer between frames.

At the same time, the contribution of the lathing cannot be separated completely from other factors. The three transverse frames did not have identical stiffness even before damage, as shown by the loading phase and later confirmed by post-test material measurements: the entrance-side tie beam showed the highest global modulus of elasticity (about 12.4 GPa), whereas the middle and laboratory-side tie beams reached about 10.0 and 9.8 GPa, respectively. The battens themselves showed a mean global modulus of about 15.2 GPa and a 5% quantile of bending strength of 69.7 MPa (Tab. 7). The observed redistribution should therefore be interpreted as the response of the complete three-frame configuration, jointly controlled by lathing, joint behaviour, support conditions, and frame-to-frame stiffness differences.

This interpretation is consistent with timber-system studies showing that secondary or strengthening elements may alter global response and residual load paths after local damage (Fragiacomo et al. 2011, Valipour et al. 2015, Rug and Schober 2015). It is also compatible with experimental work on truss joints, reinforced trusses, and semi-rigid timber connections, in which overall behaviour depends on the interaction among members, joints, and secondary elements rather than on isolated member resistance alone (Moya and Tenorio 2017, Yang et al. 2020, Neusch et al. 2022, Munafò et al. 2015). In the companion numerical calibration developed in the broader doctoral study, increasing cut depth was likewise accompanied by increasing stresses in the battens, which supports the interpretation drawn from the physical test (Martinkovičová 2025). For timber roof systems specifically, robustness and residual load paths after local damage have been addressed by Dietsch and Munch-Andersen (2011) within the robustness-assessment framework of Sørensen (2011).

## CONCLUSIONS

The experiment confirmed that the selected combination of photogrammetric measurement and inductive displacement sensors is suitable for monitoring both global and local response of a timber roof-truss model during loading, sustained full load, and progressive failure. In the direct comparison at the tie-beam midspans, the mean absolute difference between the inductive records and the averaged optical values ranged from 0.07 to 0.40 mm, while the maximum point-wise difference reached 1.39 mm for the most distant marker.

During the loading stages, the central transverse frame showed the largest vertical displacement, while the horizontal displacement of the model remained small. This indicates that the specimen behaved as a spatially interacting system with different stiffness of individual frames rather than as three isolated planar frames. During progressive cutting of the central tie beam, additional settlement relative to step 19 reached 4.28 mm and 3.97 mm in the two intact side frames at the moment of full cut, while the middle frame increased by 44.67 mm. This demonstrates measurable longitudinal load redistribution through the lathing. After complete failure of the central tie beam, the model remained temporarily self-supporting. The entrance-side frame became decisive only after the additional half-cut of the edge tie beam, which underlines the redundancy of the three-frame segment.

In the present laboratory configuration, the results indicate that lathing can act as a structurally relevant longitudinal load-transfer path when local damage is assessed. Because the specimen was simplified and tested as a single laboratory model, the findings are best interpreted as mechanism-based evidence and as a basis for subsequent detailed evaluation and numerical interpretation.

## ACKNOWLEDGMENTS

The research was supported from the project "Wooden structures prevention and maintenance for heritage conservation purposes" (NAKI III, reg. No. DH23P03OVV005), provided by the Ministry of Culture of the Czech Republic.

## REFERENCES

1. Binda, L., Saisi, A., 2005: Investigation strategies for the diagnosis of historic structures. Construction and Building Materials 19(8): 609–619.
2. Branco, J.M., Cruz, P.J.S., Piazza, M., 2014: Assessment, diagnosis and strengthening of timber structures. Construction and Building Materials 58: 1–13.
3. Bradski, G., 2000: The OpenCV library. Dr. Dobb's Journal of Software Tools 25(11): 120–125.
4. Dietsch, P., Munch-Andersen, J., 2011: Robustness of large-span timber roof structures - Two examples. Engineering Structures 33(11): 3113–3117.
5. Dinehart, D.W., Shenton, H.W., 1998: Experimental testing of timber trusses. Journal of Structural Engineering 124(2): 123–130.
6. Fassi, F., Achille, C., Fregonese, L., Adami, A., 2013: Photogrammetry for structural monitoring. ISPRS Annals of the Photogrammetry, Remote Sensing and Spatial Information Sciences II-5/W1: 115–122.
7. Fragiacomo, M., Amadio, C., Macorini, L., 2011: Load distribution in timber structures. Engineering Structures 33(2): 399–407.
8. Frese, M., Blass, H.J., Schädle, P., 2012: Full-scale testing of timber structures. Engineering Structures 40: 457–466.
9. Garrido-Jurado, S., Muñoz-Salinas, R., Madrid-Cuevas, F.J., Marín-Jiménez, M.J., 2014: Automatic generation and detection of highly reliable fiducial markers under occlusion. Pattern Recognition 47(6): 2280–2292.
10. Hu, J., Liu, E., Yu, J., 2021: Application of structural deformation monitoring based on close-range photogrammetry technology. Advances in Civil Engineering 2021: Article ID 6621440.
11. Jasieńko, J., Nowak, T., Bednarz, Ł., 2016: Failure analysis of historical timber structures. Materials and Structures 49: 123–134.
12. Kunecký, J., Sebera, V., Hasníková, H., Arciszewska-Kędzior, A., Tippner, J., Kloiber, M., 2015: Experimental assessment of a full-scale lap scarf timber joint accompanied by a finite element analysis and digital image correlation. Construction and Building Materials 80: 24–33.

13. Li, H., Dai, Y., Qiu, H., He, X., 2022: Application of multi-camera digital image correlation in the stability study of the long timber column with the circular cross-section under axial compression. BioResources 17(1): 1717–1728.
14. Luhmann, T., Robson, S., Kyle, S., Harley, I., 2013: Close-range photogrammetry and 3D imaging. 2nd ed. De Gruyter. Pp. 684.
15. Martinkovičová, S., 2025: Vybrané problémy modelovania historických krovov (Selected issues in the modelling of historical roof trusses). Doctoral thesis (in Slovak). Slovak University of Technology in Bratislava, Faculty of Civil Engineering, Bratislava. Pp. 124. https://opac.crzp.sk/?fn=detailBiblioForm&sid=BA75C2D62745AD5722E4929ED92F
16. Martinkovičová, S., Sandanus, J., Brodniansky, J., Ondrašinová, L., 2025: Static analysis of selected types of roof trusses considering the weakening of the structural elements. Slovak Journal of Civil Engineering 33(3): 47–53.
17. Mills, J., Barber, D., Bryan, P., 2010: Metric survey for structural analysis of historic buildings. Journal of Architectural Conservation 16(3): 7–22.
18. Moya, R., Tenorio, C., 2017: Strength and displacement under tension and compression of wood joints fastened with nails and screws for use in trusses in Costa Rica. Wood Research 62(1): 139–156.
19. Munafò, P., Stazi, F., Tassi, C., Davì, F., 2015: Experimentation on historic timber trusses to identify repair techniques compliant with the original structural-constructive conception. Construction and Building Materials 87: 54–66.
20. Neusch, M., Sandanus, J., Freudenberger, K., 2022: Experimental verification of the modern semi-rigid timber connections. Wood Research 67(6): 1005–1016.
21. Nowak, T., Jasieńko, J., Bednarz, Ł., 2013: Failure mechanisms of timber roof trusses. Engineering Structures 52: 1–10.
22. Özkan, T., Pfeifer, N., Styhler-Aydın, G., Hochreiner, G., Herbig, U., Döring-Williams, M., 2022: Historic timber roof structure reconstruction through automated analysis of point clouds. Journal of Imaging 8(1): 10.
23. Remondino, F., 2011: Heritage recording and 3D modeling with photogrammetry. Remote Sensing 3(6): 1104–1138.
24. Reynders, E., Wursten, G., De Roeck, G., 2010: Structural health monitoring of civil engineering structures. Mechanical Systems and Signal Processing 24(3): 611–626.
25. Ross, R.J., 2015: Nondestructive evaluation of wood. 2nd ed. Forest Products Laboratory, USDA. Pp. 176.
26. Rug, W., Schober, K.U., 2015: Load-bearing behaviour of timber trusses. Construction and Building Materials 76: 360–368.
27. Sørensen, J.D., 2011: Framework for robustness assessment of timber structures. Engineering Structures 33(11): 3087–3092.
28. Stepinac, M., Rajčić, V., Barbalić, J., 2017: Behaviour of timber structures under damage conditions. Engineering Structures 148: 62–74.
29. Valipour, H.R., Bradford, M.A., Gilbert, R.I., 2015: Load redistribution in timber structures after element failure. Construction and Building Materials 76: 412–422.
30. Yang, X., Zhao, Q., Hao, D., Wang, J., Fu, S., Ma, L., 2020: Flexural behavior of OSB reinforced wood truss. Wood Research 65(2): 245–256.

31. Yeomans, D., 2003: The repair of historic timber structures. Thomas Telford. Pp. 224.
32. Zybała, T., Szepietowska, K., Bukal, G., Lubowiecka, I., 2022: Portico farmhouses of the Vistula delta: Architecture, current state and finite element modelling of timber roof truss under material and cross-section uncertainty. International Journal of Architectural Heritage 16(12): 1885–1906.

JÁN BRODNIANSKY*, SILVIA MARTINKOVIČOVÁ, JAROSLAV SANDANUS,
TOMÁŠ KLAS
SLOVAK UNIVERSITY OF TECHNOLOGY IN BRATISLAVA
DEPARTMENT OF STEEL AND TIMBER STRUCTURES
RADLINSKÉHO 11, 810 05 BRATISLAVA
SLOVAK REPUBLIC
*Corresponding author: jan_brodniansky@stuba.sk

JIŘÍ KUNECKÝ, JIŘÍ BLÁHA, MICHAL KLOIBER
INSTITUTE OF THEORETICAL AND APPLIED MECHANICS
CZECH ACADEMY OF SCIENCES
PROSECKÁ 809/76, 190 00 PRAGUE 9
CZECH REPUBLIC